CHAPTER 10

Diffuse Optical Imaging and PET Imaging

Soren D. Konecky and Arjun G. Yodh

10.1 Introduction

In the preceding two chapters, diffuse optical imaging (DOI) was combined with magnetic resonance imaging (MRI) and X-ray imaging. The primary goal of that work was to combine higher-resolution imaging modalities with low-resolution diffuse optical imaging in order to use structural information from the former to improve upon the functional potential of DOI. In particular, the structural details acquired using MRI and X-ray imaging were used as a priori information to aid the optical reconstructions. The goal of the research described in this chapter is different. We will coregister DOI of human breast with positron emission tomography (PET). PET is a clinically useful imaging modality that employs the uptake of radiopharmaceuticals to measure physiological processes. In PET, the increased metabolic rate of most tumors compared to normal tissue provides a basis for their detectability via the radiopharmaceutical ^{18}F-fluorodeoxyglucose (^{18}F-FDG). Like PET, DOI also primarily measures the physiological characteristics of tissue. DOI is sensitive to changes in the absorption of near-infrared light due to variation of the concentrations of endogenous chromophores such as oxy- and deoxyhemoglobin, water, and lipid. Using exogenous fluorescence probes, DOI also has the potential to measure other physiological characteristics of tissue such as pH, intracellular calcium concentration, and tumor specific receptors. Thus, the combined use of DOI, fluorescence DOI (FDOI), and PET holds potential to expand the toolbox for researchers who study cancer in vivo. The goal of this chapter is to compare PET and DOI for breast tumor imaging, to demonstrate how these comparisons can be accomplished, and to suggest ways that the coregistration of these functional imaging techniques may be beneficial.

We begin by reviewing some research in both the PET and DOI literature. Clearly, the ability to detect physiological change is important for measuring and predicting tumor responses to cancer treatment. To date, clinicians primarily use tumor size to evaluate the response of tumors to therapy. Unfortunately, however, this approach requires clinicians to wait weeks to months for anatomical changes to occur, even though some physiological changes surely occur on shorter timescales. In addition, some of the newest therapies (e.g., hormone therapies for breast cancer) are potentially "cytostatic." These therapies may stop cancer growth without destroying the cancer and may be successful even when no significant reduction in

tumor size occurs [1]. So while tumor size will always be important in evaluating treatment response, there is a need to predict and monitor cancer therapy on shorter timescales. PET scans taken after the first round of chemotherapy are demonstrably strong indicators of treatment efficacy in breast cancer patients [2–7]. Likewise, several case studies using optical methods to monitor neoadjuvant chemotherapy of locally advanced breast cancers have shown promise [8–10]. Unlike PET, continuous or repetitive treatment monitoring is feasible with optics due to its low cost and noninvasive nature. In all of these studies, the long-term clinical goal is to predict the outcome of treatment early on, while there remains enough time to modify treatment. This is especially important for breast cancer, where many treatment options can exist, even if the initial chemotherapy fails.

DOI and PET can identify resistance factors to cancer treatments. For example, hypoxic tumors [i.e., those having a low partial pressure of oxygen (pO_2)] are often more resistant to radiation and chemotherapy [11–14]. Several studies report that the determination of the oxygenation status of a tumor might afford improved disease management [15–18]. DOI detects tumor hypoxia by measuring decreases of tissue blood oxygenation (StO_2), and high/low values of StO_2 in a lesion with respect to the surrounding tissue imply high/low relative values of pO_2 in the lesion. Likewise, increased ^{18}F-FDG uptake measured with PET is associated with hypoxia. A lack of oxygen can lead to the anaerobic metabolism of glucose, which is inefficient and requires that cells increase glucose consumption. Thus, ^{18}F-FDG uptake could be correlated with tissue StO_2.

There are further potential benefits to be derived by combining DOI and PET. DOI data can facilitate more accurate determination of the tumor hypoxic state by PET. Some nonhypoxic tumors have high rates of glucose metabolism, and chronic hypoxia can lead to decreases in glucose metabolism. ^{18}F-FDG PET alone is therefore not always a reliable measure of tissue hypoxia. Indeed, this observation has lead to recent research using nitroimidazole PET tracers such as ^{18}F-fluoromisonidazole to measure tumor hypoxia in variety of cancers, including breast cancer [19, 20]. Diffuse optical methods measure tissue oxygenation using endogenous contrast. Thus, they are not subject to variations in tracer uptake due to physiological factors such as poor perfusion [21]; nor do they require the subject to return to the hospital on another day for injection and scan of a second tracer. In addition, simple models of the relative rate of oxygen metabolism in tumors can be employed by diffuse optical methods [22] and might in the future provide a means to study the relationship between FDG kinetics and oxygen metabolism. A high rate of glucose consumption that is not accompanied by a high rate of oxygen metabolism, for example, would imply that some glucose is being metabolized inefficiently, presumably due to an insufficient supply of oxygen.

Finally, PET techniques are well suited to validate DOI. This validation is important because, unlike PET, DOI is still in its initial research phase and has not as yet been fully translated to the clinic. It is reasonable to expect that increases in glucose metabolism require more blood for glucose and oxygen delivery and therefore should be accompanied by increases in total hemoglobin concentration. In fact, ^{18}F-FDG uptake has already been shown to correlate well with the uptake of a tumor blood-flow-specific tracer in breast cancer [23, 24]. If a strong correlation between

hemoglobin concentration and glucose consumption exists, PET could be very well suited to validate DOI results.

The remainder of this chapter is organized as follows. We begin with an introduction to PET imaging for researchers in optical imaging. This is followed by sections on DOI and fluorescence DOI, with an emphasis on the methods used in recent work. Next, we show results from recent clinical research. Comparisons between DOI and PET imaging for breast cancer suggest correlations between ^{18}F-FDG uptake and optically measured parameters such as total hemoglobin concentration and scattering [25]. Fluorescence DOI (FDOI) of human breast using indocyanine green (ICG) suggests increased vascular permeability in breast cancers [26].

10.2 Positron Emission Tomography (PET)

10.2.1 PET Fundamentals

Positron emission tomography (PET) is a clinically accepted imaging modality that images the uptake of a pharmaceutical of physiological interest by tagging it with a positron emitting radioisotope. The tagged pharmaceutical, called a radiopharmaceutical, is injected or inhaled. It then distributes in the body in accordance with the biokinetics of the pharmaceutical, which are similar to those of its nonradioactively labeled analog. When a proton in the nucleus of the radioisotope decays into a neutron, it emits a positron and an antineutrino. The positron travels a short distance (~1 mm for ^{18}F) in the tissue losing energy through Coulomb interactions, and eventually annihilates with an electron. The annihilation produces a pair of 511-keV photons traveling in (nearly) opposite directions [Figure 10.1(a)]. Assuming neither photon is absorbed by tissue, the two photons will exit the body at almost the exact same time. PET tomographs are designed to detect these coincident photon pairs along all possible projection lines through the body [Figure 10.1(b)]. By measuring the number of photon pairs emitted along each projection line, one can reconstruct quantitative maps of the tracer distribution. The resulting image of tracer distribu-

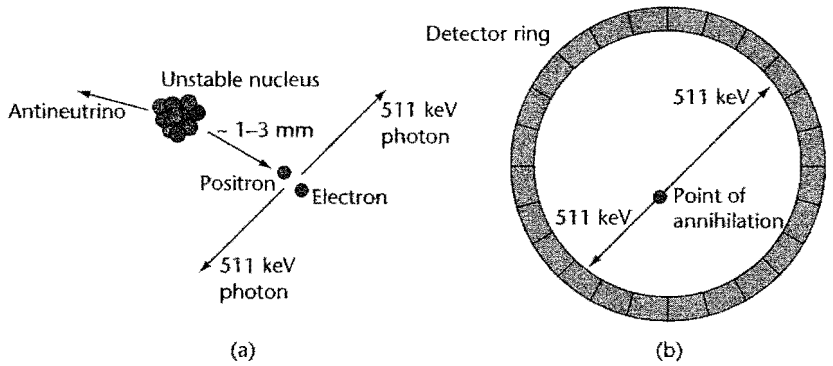

Figure 10.1 (a) Schematic of positron decay and annihilation. A proton in the unstable nucleus decays to neutron giving off a positron and antineutrino. The positron travels a few millimeters in tissue before annihilating with an electron to give off a pair of 511-keV photons traveling in opposite directions. (b) An annihilation event produces two 511-keV photons, which are detected by a ring of detectors.

tion thus serves as an indication of a physiologic process, which is interpreted by the physician.

The tracer used for most clinical studies is ^{18}F-fluorodeoxyglucose (^{18}F-FDG). As ^{18}F has a half-life of 109.8 minutes, a relatively large fraction of the ^{18}F decays may be detected during a typical 30-minute scan. In addition, the half-life is long enough so that the radioactive fluorine can be produced in a regional facility and flown to nearby hospitals. An analog of glucose, ^{18}F-FDG enters the cell and is phosphorylated in parallel to glucose to form ^{18}F-fluorodeoxyglucose-6-phosphate (^{18}F-FDG-6-P). However, once phosphorylated, it cannot be further broken down by the cell. Furthermore, the ^{18}F-FDG-6-P is not readily dephosphorylated and cannot cross the cell membrane. As a result, the ^{18}F-containing molecule is metabolically trapped in the cell. Over time, cells metabolizing larger amounts of glucose will accumulate more ^{18}F. An image of the ^{18}F distribution in the body taken about an hour after injection offers a quantitative mapping of ^{18}F-FDG uptake. It is therefore a good measure of glucose metabolism.

10.2.2 PET Image Reconstruction

Image-reconstruction methods in PET can be divided into two general categories: analytic and iterative (see [27, Chs. 21 and 22], for a more in-depth treatment). In the analytic approaches, the data for each pair of detectors (corrected for attenuation) is treated as the radon transform (line integral) of the tracer concentration across the line connecting the two detectors. The tracer concentration is determined by inverting the radon transform using filtered back-projection or a related algorithm. Analytic methods are computationally fast; however, they do not permit all effects of the measurement process to be modeled.

Iterative methods require a large amount of computation but permit more accurate modeling of the measurement process. These methods involve the inversion of a system matrix (similar to the weight matrix in DOI), which gives the sensitivity of each measurement to each voxel in the image. Unlike the weight matrix in DOI, however, the system matrix for PET is linear (i.e., the values of its elements do not depend on the tracer distribution for which we are solving). Also, in contrast to optical tomography, where the weight matrix is nearly singular, for most detector configurations, the PET system matrix is well posed and easily inverted. Each row corresponds to one detector pair and consists primarily of ones for voxels in a narrow volume connecting the pair of detectors and zeroes for other voxels, with adjustments that take into account the attenuation and scattering of the 511-keV photons, random coincidence events, and detector characteristics.

The principal difficulty in PET reconstructions is that only a small number of photons are collected. As a result, the data is noisy, and it is desirable to take into account photon statistics of the measurement. For this reason the system matrix is inverted using iterative algorithms that attempt to find the tracer distribution with the highest probability for producing the measured data. The maximum-likelihood expectation-maximization (ML-EM) algorithm, first used in emission tomography in the 1980s, is the best known [28, 29]. Several other algorithms have been developed to speed up the slow convergence of the ML-EM algorithm when reconstructing large 3D volumes. One of these, the three-dimensional row-action maximum

likelihood algorithm (3D RAMLA), was used to generate the PET reconstructions for the work presented in this chapter [30].

10.2.3 PET Instrumentation

We will compare 3D DOI reconstructed breast images with PET images of the same breast acquired by two different PET scanners: a dedicated breast-only PET (BPET) scanner developed at the University of Pennsylvania and a commercially available whole-body PET scanner (Allegro, Philips Medical Systems). We briefly describe the scanners here. For a thorough discussion of PET system design, the reader is referred to the review by Lewellen and Karp [27, Ch. 10].

Commercially available whole-body PET tomographs achieve high sensitivity to 511-keV annihilation photon pairs using a cylindrical configuration of detectors surrounding the patient. The imaging instrument used for acquisition of whole-body PET images in this chapter was an Allegro scanner, with an axial field of view (FOV) of 18 cm, a transaxial FOV of 56 cm, and a ring diameter of 86.4 cm at the surface of the detectors. The scanner exhibits 5-mm spatial resolution (i.e., FWHM of a point source) and a sensitivity of 4.4 cps/kBq [31].

In our study, patients fasted for at least 4 hours prior to the scan. Each scan was initiated 60 minutes after intravenous administration of ^{18}F-FDG with a dose of 5.2 MBq/kg. Sequential overlapping scans were acquired to cover the body from neck to pelvis as the patient lay supine on the gantry. Transmission scans obtained with a ^{137}Cs point source were interleaved between the multiple emission scans to correct for nonuniform attenuation of the 511-keV photons by the patient's body and the gantry.

The ability to image breast cancer with ^{18}F-FDG PET has led to the development of a dedicated breast-imaging PET scanner, BPET [32, 33]. In a whole-body scanner, the 511-keV photons emitted from the breast are attenuated by the body, reducing the scanner's sensitivity to breast lesions. In contrast, a dedicated breast scanner permits the breast to be imaged with significant reduction in attenuation (i.e., about a factor of 10 reduction). The subject lies prone on a table with an opening to allow the breast to drop between two detectors whose separation distance can be adjusted to accommodate different-sized breasts [Color Plate 23(a)].

The scanner is composed of two curved-plate NaI(Tl) detectors of 1.9-cm thickness each with an active area of 28×21 cm^2. By positioning the detectors close to the breast, a large solid angle can be covered, thus optimizing the system's sensitivity for a split-ring configuration. However, this configuration leads to the loss of data from the 511-keV photons arriving at angles not covered by the detector plates. In fact, for a typical separation of 20 cm, the angular coverage of 180° corresponds to one-half of the complete angular acceptance. This geometry requires the use of a limited angle reconstruction, which we perform using a modified version of 3D RAMLA that compensates for the missing data.

The spatial resolution of the system varies from 3.8 mm (radially at center) to 4.5 mm (radially at $r = 5$ cm). The Allegro whole-body scanner has a uniform spatial resolution of 5 mm. Phantom measurements have demonstrated superior contrast recovery for BPET compared to the Allegro instrument as a result of the improved spatial resolution, even with the loss of data due to the limited angle geometry. A

pilot study of 20 patients imaged with both Allegro and BPET demonstrated good correlation in lesion detectability, but better detail in the breast lesions was achieved in the BPET images [34].

10.3 Diffuse Optical Imaging (DOI)

10.3.1 DOI Instrumentation

There are two basic approaches for combining diffuse optical measurements with measurements from other medical imaging modalities. In one approach the DOI device is incorporated into the other device. This approach was described in Chapter 6 by Carpenter and Pogue (MRI) and in Chapter 9 by Fang, Carp, Selb, and Boas (X-ray tomosynthesis) [35–38]. The advantage of such a system is that measurements from the two modalities can be made concurrently in the same geometry, facilitating coregistration of the resulting images. However, integration of the DOI system into another instrument places restrictions on both instrumentation types. In the second approach, measurements are taken on separate stand-alone devices. Parameters are derived optimally from the respective images (taken separately) and compared. Then, as described by Azar in Chapter 7, software can be used to coregister the images for a more detailed comparison. This approach readily permits DOI measurements to be combined with more than one modality.

Our DOI imaging device is a hybrid system [Color Plate 23(b)]. The instrument takes both continuous-wave transmission and frequency-domain remission measurements at six near-infrared wavelengths in the parallel-plate soft-compression geometry. The patient lies in a prone position with her breasts inside a box with an antireflection coated glass window on the detector side. A compression plate holds the breast in place against the viewing window by mildly compressing the breast to a thickness of between 5.5 and 7.5 cm. The box is then filled with a matching fluid with optical properties similar to human breast. The matching fluid consists of water, India ink for absorption, and a fat emulsion for scattering.

Six diode lasers (650, 690, 750, 786, 830, and 905 nm), four of which (690, 750, 786, and 830 nm) are intensity-modulated at 70 MHz, are connected via optical fibers and series of optical switches (DiCon Fiber Optics, Richmond, California) to 45 source positions located on the compression plate. The source positions form a 9×5 grid with a separation of 1.6 cm between nearest neighbors. The breast is scanned by serially guiding the light from each laser to each source position.

For remission detection, nine homodyne frequency-domain detector units [39] are connected to the compression plate by a 3×3 grid of 3-mm detector fibers with a spacing of 1.6 cm. Each unit contains an avalanche photodiode and utilizes a homodyne technique to derive the amplitude and phase of the detected signal. For transmission detection, a CCD camera (Roper Scientific, Trenton, New Jersey, VersArray:1300F) is focused on the viewing window. It acquires an image for each source-position/laser combination with an exposure time of 500 ms. A 24×41 grid of 984 pixels is selected from the CCD chip. It measures the continuous wave light intensity at locations on the viewing window with a spacing of ~3 mm.

10.3.2 DOI Image Reconstruction

Our multispectral approach permits us to solve directly for oxy- and deoxyhemoglobin concentrations via decomposition of the absorption coefficient into contributions from individual chromophores, assuming a simple Mie-scattering approximation for the reduced scattering coefficient. We implemented this approach by modifying the Time-resolved Optical Absorption and Scattering Tomography (TOAST) software in order to utilize multispectral continuous wave data [40]. The method is described in detail in Corlu et al. [41].

The propagation of near-infrared light in biological media is modeled by a diffusion equation [42]. In the frequency domain, the equation has the form

$$-\nabla \cdot D(\mathrm{r},\lambda)\nabla\Phi(\mathrm{r},\lambda,\omega)+\left[\mu_a(\mathrm{r},\lambda)+\frac{i\omega n}{c}\right]\Phi(\mathrm{r},\lambda,\omega)=q_0(\mathrm{r},\lambda,\omega) \tag{10.1}$$

Here Φ is the photon fluence rate, λ is the wavelength of the light source, ω is the frequency at which the light source is intensity-modulated ($\omega = 0$ for continuous-wave measurements), q_0 is the light source distribution, and c is the speed of light. The optical properties of the breast are described by the light diffusion coefficient $D \approx 1/3\mu_s'$ (μ_s' is the reduced scattering coefficient), the absorption coefficient μ_a, and the tissue index of refraction n.

We model the absorption coefficient as the sum of the absorption from the individual chromophores (Hb, HbO_2, water, and lipids) in the breast, that is,

$$\mu_a(\lambda)=\sum_i c_i\varepsilon_i(\lambda) \tag{10.2}$$

Here, each c_i is the concentration of the ith chromophore, and $\varepsilon_i(\lambda)$ is the corresponding wavelength-dependent extinction coefficient. We model the wavelength dependence of the reduced scattering coefficient using simplified Mie scattering theory [43, 44]. A scattering prefactor, A, depends primarily on the number and size of the scatterers, and a scattering exponent, b, depends on the size of the scatterers. They are combined as follows:

$$\mu_s' = A\lambda^{-b} \tag{10.3}$$

Our goal is to reconstruct spatial maps of A, b, and the chromophore concentrations by minimizing the difference between measured data and predictions of the photon diffusion model.

Two scans are made for each breast: a reference scan in which the tank is filled with matching fluid only and a scan with the breast immersed in matching fluid. We fit data from the frequency-domain measurements of the breast to an analytic solution of the diffusion equation for a homogeneous medium in the slab geometry in order to obtain estimates of the average chromophore concentrations, scattering prefactor A, and scattering power b inside the breast. The absorption due to volume concentrations of water (31%) and lipid (57%) in the breast is held fixed, based on values from the literature [45–47]. The optical properties of the matching fluid are determined independently by fitting to the frequency-domain measurements of the reference scan.

A photograph of the compressed breast is taken just before the scan. It allows us to segment the imaging volume into breast and matching fluid regions. Using average results for the breast as an initial guess, we then employ a nonlinear conjugate gradient algorithm to solve directly for 3D tomographic maps of the chromophore concentrations and scattering prefactor A inside the breast. The scattering amplitude b is held fixed at its bulk value, as are the optical properties of the matching-fluid region. At each iteration, a finite element solver predicts the detected continuous-wave light intensity based on the current maps of chromophore concentrations, and these maps are then updated in order to minimize χ^2, which represents the difference between measured and predicted values of light exiting the breast. Finally, the resulting maps are combined to form images of total hemoglobin concentration $[THC(\mathbf{r}) = C_{Hb}(\mathbf{r}) + C_{HbO_2}(\mathbf{r})]$, blood oxygen saturation $[StO_2(\mathbf{r}) = C_{HbO_2}(\mathbf{r})/THC(\mathbf{r})]$, reduced scattering coefficient $[\mu_s'(\mathbf{r}) = A(\mathbf{r})\lambda^{-b}]$, overall optical attenuation $[\mu_{eff}(\mathbf{r}) = \sqrt{\mu_a(\mathbf{r})/D(\mathbf{r})}]$, and an empirical optical index $[OI(\mathbf{r}) = rTHC(\mathbf{r}) \times r\mu_s'(\mathbf{r})/rStO_2(\mathbf{r})]$.

10.4 Fluorescence Diffuse Optical Imaging (FDOI)

The use of exogenous contrast agents holds potential to increase the number of physiological parameters that can be measured by diffuse optical methods. Fluorescent contrast agents have been used to measure tissue pH [48], intracellular calcium concentration [49], and a variety of tumor-specific receptors [50–56]. Many researchers have explored the use of fluorescence imaging in turbid media [57–61]. Because it is approved by the FDA, the most widely used contrast agent in the diffuse optics community has been indocyanine green (ICG). Several studies suggest that leaky vasculature in tumors delays the washout of ICG, raising the relative concentration between cancerous and normal tissue [35, 62, 63].

In our experiments, an additional ICG fluoresence scan is performed after the endogenous optical properties of the breast are measured using the methods described in Section 10.3. The fluorescence scan is performed with 786-nm excitation light. An 830-nm bandpass filter (OD = 4, CVI Laser Inc.) and a 785-nm notch filter (OD = 6, Semrock, Inc.) are placed in front of the CCD. The notch filter is put in front of the bandpass filter. In this way, the 786-nm excitation light is blocked before reaching the bandpass filter, preventing the detection of excitation-light-induced bandpass filter autofluorescence. The total extinction of 785-nm excitation light is 10 dB, and the transmission loss of 830-nm emission light is approximately 50% (mostly due to the bandpass filter).

The protocol for the fluorescence scan is as follows. A monitoring scan consisting of repeated measurements using a single source position begins 45 seconds before the administration of ICG. This scan is used later to derive the ICG pharmacokinetics. A bolus of sterile ICG is then given for 30 seconds, followed by a normal saline flush of 20 cc for 30 seconds. After 24 frames (i.e., 6 minutes) of the monitoring scan, a full tomographic scan using all 45 source positions (including the one used in the monitoring scan) is conducted.

For fluorescence image reconstruction, we attempt to determine the spatially varying concentration of fluorophore in the sample. The transport of the emitted light is governed by (10.1) at the emission wavelength. For a continuous-wave measurement ($\omega = 0$), the concentration of fluorophore is related to the source term on the right side of this equation by

$$q_0(\lambda_{fl}, \mathbf{r}) = C(\mathbf{r}) \times \varepsilon(\lambda_{ex}) \times \eta \times \Phi(\lambda_{ex}, \mathbf{r}) \tag{10.4}$$

That is, the amount of fluorescent light emitted $q_0(\lambda_{fl}, \mathbf{r})$ is proportional to the product of the fluorophore concentration $C(\mathbf{r})$ and the amount of excitation light $\Phi(\lambda_{ex}, \mathbf{r})$. The amount of excitation light inside the medium can be calculated by solving the diffusion equation with, for example, finite element methods using the reconstructed values of $\mu(\lambda_{ex}, \mathbf{r})$ and $\mu_s'(\lambda_{ex}, \mathbf{r})$ determined from the endogenous scan. (Here we are typically ignoring the small extra absorption due to the fluorescent probe.) The proportionality constants are the extinction coefficient $\varepsilon(\lambda_{ex})$ and the fluorescence quantum yield η of the fluorophore.

To solve for the fluorophore concentration, we convolve the source term (10.4) with the Green's function for the diffusion equation (10.1) given the optical properties of the medium. Since the excitation and emission wavelengths are close, it is a reasonably good approximation to use the optical properties determined at the excitation wavelength from the endogenous image reconstruction. Thus, the equation we must solve is

$$\Phi_m(\lambda_{fl}, \mathbf{r}_s, \mathbf{r}_d) = \int d^3 r \Phi_c(\lambda_{ex}, \mathbf{r}_s, \mathbf{r}) G_c(\lambda_{ex}, \mathbf{r}, \mathbf{r}_d) \varepsilon(\lambda_{ex}) \eta C(\mathbf{r}) \tag{10.5}$$

It is common to account for systematic errors (e.g., varying detector efficiencies and light strengths between different source/detector pairs) by multiplying the measured emission data by the calculated excitation data divided by the measured excitation data [i.e., $\Phi_c(\lambda_{ex}, \mathbf{r}_s, \mathbf{r}_d)/\Phi_m(\lambda_{ex}, \mathbf{r}_s, \mathbf{r}_d)$] [64]. In addition, it is necessary to scale the emission data to account for the ICG washout that occurs during the (10-minute) fluorescence scan. Ideally, the scaled data should represent the signal that would be measured if the emission light for all the source positions could be measured at the same time. The scaling can be accomplished by monitoring the ICG kinetics using a single source position as described above, then fitting the measured fluorescent signal to a decaying exponential. For each CCD exposure, the measured value for all pixels is multiplied by $\exp[\beta(t_i - t_0)]$ where β is the decay rate of the monitored fluorescence signal, t_i is the time at which source i is measured, and t_0 is the time at which we are solving for the fluorophore concentration $C(\mathbf{r})$ [63].

Once the raw emission data has been adjusted, the simplest approach is to divide the sample into voxels with volume h^3, discretize (10.5), and solve the resulting matrix equation. For each measurement i and voxel j in the medium, we let

$$A_{i,j} = h^3 \Phi_c(\lambda_{fl}, \mathbf{r}_{si}, \mathbf{r}_j) G_c(\lambda_{fl}, \mathbf{r}_j, \mathbf{r}_{di}) \varepsilon(\lambda_{ex}) \eta \tag{10.6}$$

$$x_j = C(\mathbf{r}_j) \tag{10.7}$$

and

$$b_i = \frac{\Phi_c(\lambda_{ex}, \mathbf{r}_{si}, \mathbf{r}_{di})}{\Phi_m(\lambda_{ex}, \mathbf{r}_{si}, \mathbf{r}_{di})} \Phi_m(\lambda_{fl}, \mathbf{r}_{si}, \mathbf{r}_{di}) \tag{10.8}$$

We then solve the matrix equation

$$(\mathbf{A}^T\mathbf{A} + \alpha\mathbf{L})\mathbf{x} = \mathbf{A}^T\mathbf{b} \tag{10.9}$$

to get the fluorophore concentration for each voxel. The regularization term $\alpha\mathbf{L}$ can take many forms. In our reconstructions, α is constant, and $\mathbf{L}$ is a Laplacian matrix (for details, see [63, 65]).

In order for FDOI to be successful, the amount of detected emission light must be much greater than the amount of excitation light that is still detected. That is, we require that

$$\frac{\Phi(\lambda_{fl}, \mathbf{r}_s, \mathbf{r}_d)}{\Phi(\lambda_{ex}, \mathbf{r}_s, \mathbf{r}_d)} E >> 1 \tag{10.10}$$

where E is the relative detection efficiency between the emission and excitation wavelengths ($E \sim 5 \times 10^9$ using the filters described earlier). The photon fluence rate at the emission wavelength can be calculated from (10.5). For simplicity, let us assume that the concentration of fluorophore is zero outside of a small region centered at $\mathbf{r}$ (e.g., outside a tumor at r), and that all spatially dependent variables in (10.5) are approximately constant in this region. The left-hand side of (10.10) then becomes approximately

$$\frac{\Phi(\lambda_{ex}, \mathbf{r}_s, \mathbf{r}) G(\lambda_{fl}, \mathbf{r}, \mathbf{r}_d) \varepsilon(\lambda_{ex}) \eta C(\mathbf{r}) V}{\Phi(\lambda_{ex}, \mathbf{r}_s, \mathbf{r}_d)} E \tag{10.11}$$

where V is the volume of this region. For ICG in water, $\varepsilon(\lambda_{ex}) = 0.254\ \text{cm}^{-1}/\mu\text{M}$ [66] and $\eta = 0.016$ [67]. For a source/detector pair located directly across from each other through a slab of thickness $L = 6$ cm, with $\mu_a = 0{:}05\ \text{cm}^{-1}$, $\mu_s' = 8\ \text{cm}^{-1}$, and a 1 cc fluorescent inclusion with an ICG concentration of 1 μM, (10.11) equals $\sim 10^7$ which is indeed > 1.

Unfortunately, this signal level also means that the amount of fluorescent emission light detected due to the fluorescent inclusion will be $\sim 10^{-3}$ less than the excitation photons detected during the endogenous scan. For this reason, the CCD exposure time must be increased from 500 ms to ~ 15 seconds for the fluorescent scan.

10.5 Clinical Observations

10.5.1 Whole-Body PET and DOI

The simplest way to compare images from two different modalities is to use stand-alone scanners, analyze the images from each modality separately, and then

compare the results. Several studies have used this approach to compare the results of diffuse optical measurements of human breast with other modalities including, MRI [8, 35, 68], X-ray mammography [69–71], and ultrasound [70, 72].

In a recent study we compared DOI and whole-body PET images from 14 subjects with breast lesions [25]. Contrast was visible in both DOI and PET images for nine subjects, in neither DOI or PET for two subjects, and in PET only for three subjects. When contrast was seen in the DOI images it always appeared in THC, μ_s', μ_{eff}, and optical index. Significant contrast was never observed in StO_2.

These results were compared with the pathology reports from biopsies taken after imaging. A summary of the results is found in Table 10.1. Of the nine subjects who showed both DOI and PET contrast, histopathology confirmed invasive ductal carcinoma (IDC) with ductal carcinoma in situ (DCIS) in seven subjects, DCIS only in one subject, and normal breast tissue in one subject. In one of the subjects with IDC, two distinct lesions were visible with PET, but only the larger one was visible with DOI. For the subject with normal breast tissue, the increase in FDG uptake was located at a previous surgical site and was due to a postexcisional inflammation. This inflammation was visible in the DOI images as well. Of the two subjects who showed neither DOI nor PET contrast, one had a possible lipoma (benign), and the other had a cyst. Of the three subjects who showed contrast in PET but not in DOI, one had IDC and DCIS, one had a cyst (superficial and probably infected), and one did not receive a biopsy after negative findings from both ultrasound and MRI. For this subject, the uptake of FDG was diffuse (i.e., no clear focus of FDG uptake was visible).

Table 10.1 Visibility of Lesions to DOI and Whole-Body PET Compared with Histopathology After Imaging

Subject	*Age*	*Days Between DOI and PET Examination*	*Visible in PET*	*Visible in DOI*	*Histopathology (type, mBR grade, size)*
1	48	4	Yes	Yes	IDC and DCIS, 3 + 3 + 3 = 9, 2 cm
2	45	0	Yes	Yes	IDC and DCIS, 3 + 3 + 3 = 9, 0.5 cm
3	39	0	Yes	Yes	IDC and DCIS, 2 + 2 + 2 = 6, 3.4 and 0.8 cm
4	44	0	Yes	Yes	IDC and DCIS, 3 + 3 + 1 = 7, 2.3 cm
5	44	0	Yes	Yes	IDC and DCIS, 3 + 2 + 2 = 7, 1.8 cm
6	51	0	Yes	No	None (superficial cyst)
7	64	0	Yes	Yes	DCIS, 0.9 cm
8	43	0	Yes	No	None (MRI and US negative results)
9	53	0	No	No	Cyst
10	59	0	Yes	Yes	Normal tissue (surgical inflammation)
11	44	0	Yes	Yes	IDC and DCIS, 3 + 3 + 3 = 9, 1.5 cm
12	50	13	No	No	Mature adipose tissue (possible lipoma)
13	61	0	Yes	No	IDC and DCIS, 1 + 2 + 1 = 4, 0.8 cm
14	37	0	Yes	Yes	IDC and DCIS, 3 + 3 + 3 = 9, 2.3 cm

IDC: invasive ductal carcinoma; DCIS: ductal carcinoma in situ. mBR grade: (modified) Bloom-Richardson grade.
Source: [25].

A quantitative comparison of tumor-to-background ratios between the DOI and whole-body PET images showed positive correlations (p value < 0.05) between FDG uptake and THC, μ_s', μ_{eff} and optical index. However, correlation coefficients for these parameters were not particularly high ($R = 0.67$–0.76). These results are summarized in Figure 10.2. Using the mean and maximum standardized uptake values for the PET scans, as opposed to tumor-to-background ratios, had little effect on the correlations with DOI parameters. Comparison of tumor-to-background ratios for both PET and DOI did not show significant correlations with age, tumor grade, or tumor size.

10.5.2 Breast-Only PET and DOI

A more rigorous approach to comparing images from different modalities is to coregister the images. Coregistration of DOI and BPET images makes possible comparison of specific regions of the BPET images with their corresponding regions in DOI images. Coregistration also enables one to determine to what extent lesions appear in the same spatial locations for the two modalities. Reconstructed DOI images have been coregistered with MRI [36, 37, 73], ultrasound [74, 75], and X-ray mammography [38, 76].

In our study comparing DOI and PET [25], we had the opportunity to coregister DOI images of three subjects with breast abnormalities with PET images acquired on the dedicated breast-only PET scanner (BPET) described in Section 10.2. As described in Section 10.3, our DOI device is a stand-alone breast imager. Thus, PET and DOI images were not acquired concurrently. Instead, they were acquired at different times and in slightly different geometries. Fortunately, the similar geometries of the scanners made coregistration possible, though the problem was made more challenging because the breast hangs freely in the BPET scanner, while in the DOI scanner, the breast is mildly compressed (to a thickness of between 5.5 and 7.5 cm). Using the methods reported in [73] (and in Chapter 7), we were able to deform the DOI breast images and align them with the BPET breast images.

The coregistered images in Figure 10.3 show qualitatively that DOI parameters (with the exception of StO_2) are above average in the ROIs determined from BPET. To confirm this observation, we performed the following analysis. For each DOI image, we calculated the average value of particular image parameters for all voxels in the entire breast and for all voxels in the ROI. The tumor-to-background ratio (TBR) is defined as the ratio of these two parameters (i.e., TBR = <roi>/<breast>). The optical index parameter shows the greatest contrast (TBR = 1.5–1.7). THC, μ_s', and μ_{eff} exhibit somewhat less contrast (TBR = 1.1–1.4), while very little variation in StO_2 is observed (TBR $\cong$ 1.0).

10.5.3 ICG Fluorescence

As mentioned previously, exogenous fluorophores expand the number of physiological parameters that can be measured with DOI and PET. One such parameter of recent interest is vascular permeability. Several studies have explored the use of ICG as a contrast agent to help the detection and imaging of breast tumors. Many rapidly growing tumors have increased vascularity and leaky blood vessels. Certain small

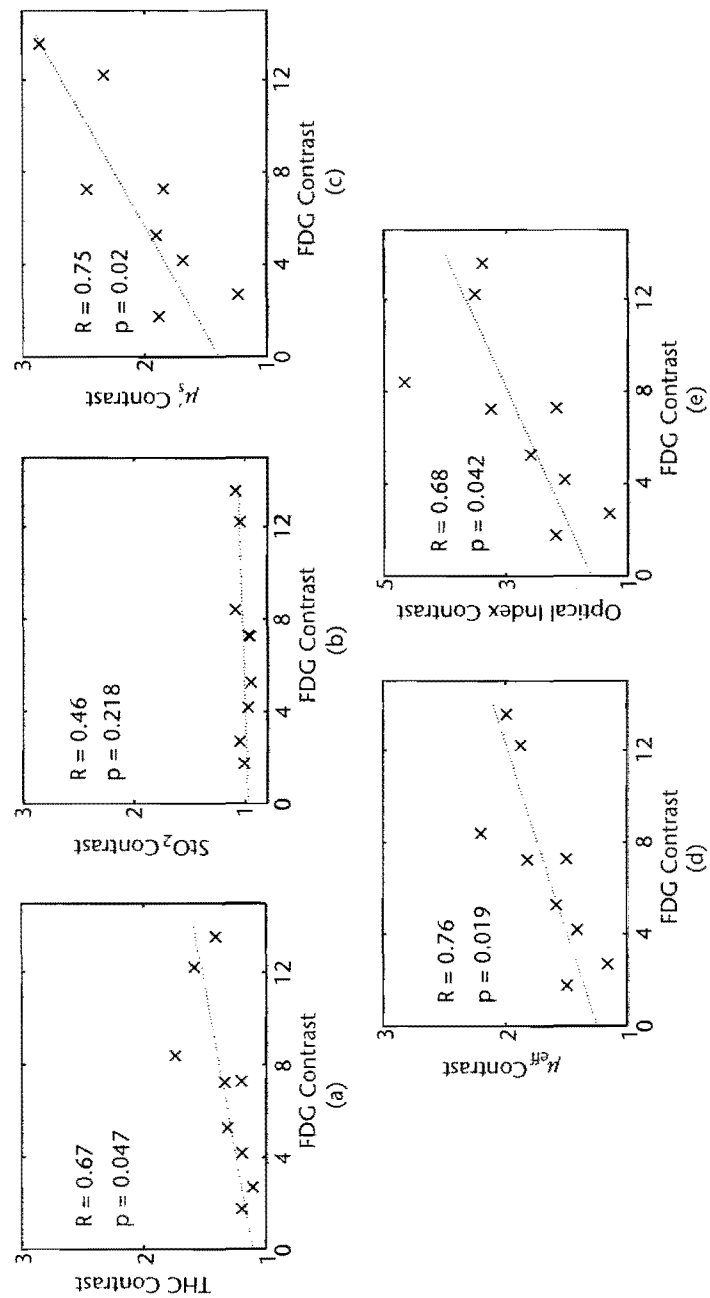

Figure 10.2 Correlations between contrast ratios in FDG uptake and DOI parameters for the nine patients with tumors visible to both DOI and PET. *R* and *p* denote the correlation coefficient and *p* value, respectively. (a) Total hemoglobin concentration (THC), (b) tissue blood oxygenation (StO_2), (c) scattering μ_s', (d) overall attenuation μ_{eff}, and (e) optical index. (*From:* [25]. © 2008 American Institute of Physics. Reprinted with permission.)

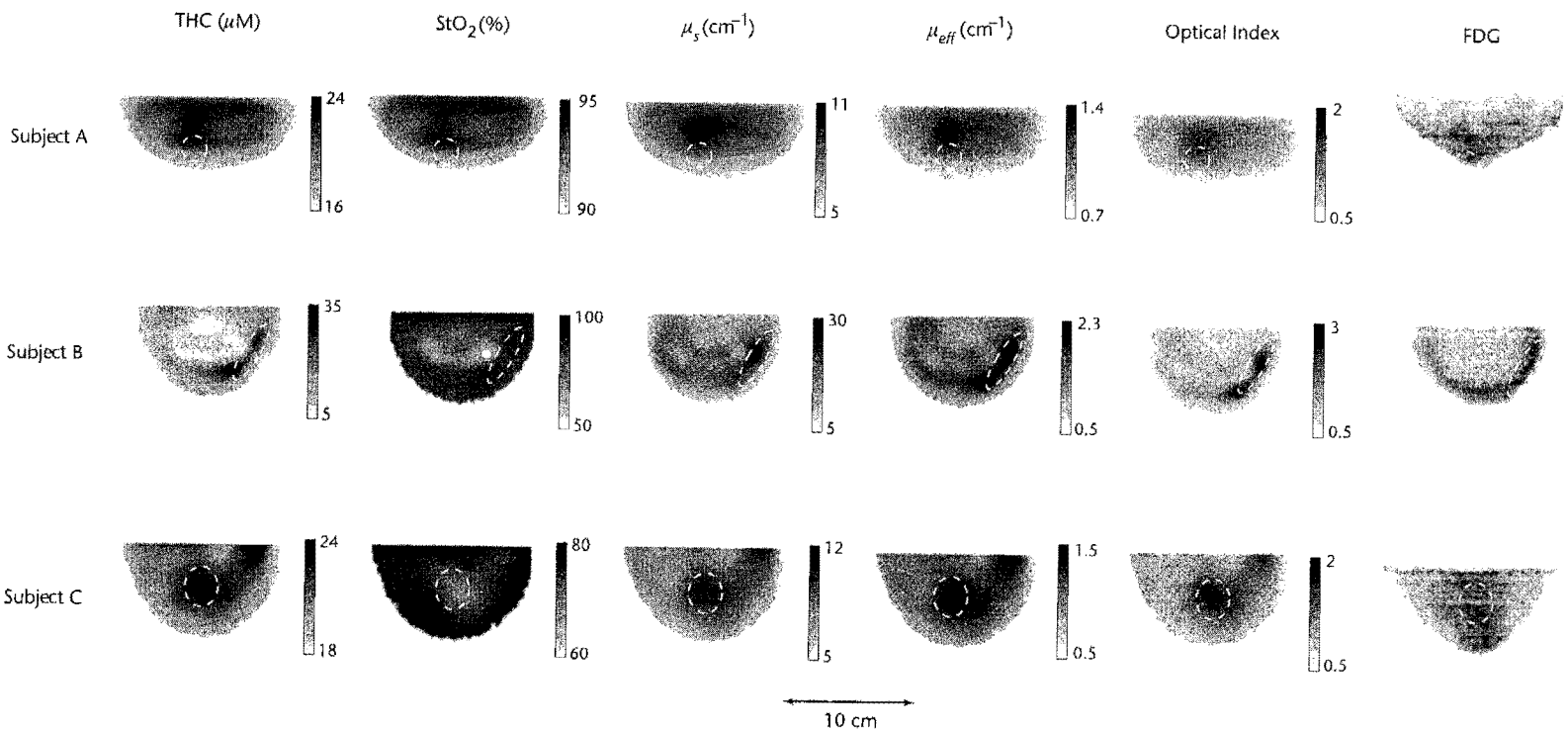

Figure 10.3 Images of the breasts from three females imaged with both DOI and BPET. Each image corresponds to a caudal-cranial slice taken from the 3D reconstruction of a breast after coregistration. Each row corresponds to a breast from one of the three patients. The columns correspond to total hemoglobin concentration (THC), tissue blood oxygenation (StO_2), reduced scattering coefficient μ_s' at 786 nm, overall attenuation (μ_{eff}), optical index, and FDG uptake measured with PET. The dashed ellipses enclose the regions of interest. (*From:* [25]. © 2008 American Institute of Physics. Reprinted with permission.)

molecules, such as the MRI contrast agent gadolinium chelate, can leak from these blood vessels and then accumulate in the intravascular space. Breast imaging with ICG is predicated on the hypothesis that ICG, a small molecule that binds to albumin in plasma, will accumulate in this space as well. Indeed, Ntziachristos et al. [35] imaged absorption contrast due to ICG in the breast of three subjects. Their measurements were made concurrently with gadolinium-enhanced MRI and exhibited agreement with respect to the localization and contrast of lesions. Intes et al. [62] were also able to localize breast tumors using ICG absorption. In addition, their research provided evidence that variation of the in vivo ICG pharmacokinetics between normal and diseased tissue may help to distinguish benign from malignant tumors.

Successful in vivo fluorescence DOI (FDOI) has been demonstrated in whole-body imaging in mice by several authors with a variety of fluorescent probes [51, 77–81]. Researchers have also explored fluorescence lymph imaging in mice [82], swine [83], and breast cancer patients [84]. Recently, Corlu et al. were able to translate FDOI into humans using ICG fluorescence to image breast tumors in three subjects [63]. Two of the three subjects were also measured using whole-body PET. The schematic in Color Plate 24(a) shows the location of an invasive ductal carcinoma in a 46-year-old premenopausal female. The tumor is clearly visible in the gadolinium-enhanced MR image [Color Plate 24(b)], which is also a measure of vascular permeability. To get a composite view of the raw data, the sum of the CCD exposures from all source positions during the fluorescent scan divided by the sum of all CCD exposures during the endogenous scan is shown in Color Plate 24(c). The right-hand side of the image corresponds to the lateral side of the right breast as viewed from the feet of the subject. Color Plate 24(d) shows an axial slice from the ^{18}F-FDG whole-body PET images of this subject. The right breast containing the tumor appears in the upper left corner. Color Plate 25(a) shows the reconstructed DOI images of this breast. The tumor is clearly visible in the total hemoglobin, reduced scattering, and ICG concentration images. However, as shown in Color Plate 25(b), the contrast in the ICG concentration image is significantly larger. ICG and ^{18}F-FDG uptake were visible in similar locations for the two subjects having both PET and FDOI scans. The maximum standardized uptake values of ^{18}F-FDG in the two subjects were 1.6 and 3.8, compared to ICG contrast ratios of 5.5 and 3.5, respectively. Further work is needed in order to determine what relationship, if any, exists between ICG contrast and the uptake of ^{18}F-FDG.

10.6 Summary

PET, DOI, and FDOI are functional imaging techniques that interogate cancer physiology in deep tissue in vivo. Combined, they have the potential to measure a large number of functional parameters. Among these parameters, glucose metabolism, hypoxia, tissue hemoglobin concentration and saturation, tissue scattering, and vascular permeability were explored in this chapter. This work, the first to explore the potential of PET and DOI multimodal imaging, will likely stimulate further investigation along these lines for cancer-response characterization.

Acknowledgments

We wish to thank our PET collaborators R. Wiener, S. M. Srinivas, J. R. Saffer, R. Freifelder, and J. S. Karp. We also thank N. Hajjioui, A. Khamene, and F. Azar for developing the software used to coregister DOI and PET images. For patient recruitment, we thank M. D. Schnall, M. A. Rosen, B. J. Czerniecki, and J. C. Tchou. Finally, this work would not have been possible without the contributions of DOI researchers R. Choe, A. Corlu, T. Durduran, K. Lee, David Busch, M. Schweiger, S. R. Arridge, and M. Grosicka-Koptyra.

References

[1] Eubank, W. B., and D. A. Mankoff, "Evolving role of positron emission tomography in breast cancer imaging," *Sem. Nucl. Med.* 35 (2005): 84–99.

[2] Schwarz, J. D., et al., "Early prediction of response to chemotherapy in metastatic breast cancer using sequential ^{18}F-FDG PET," *J. Nucl. Med.* 46 (2005): 1144–1150.

[3] Smith, I. C., A. E. Welch, A. W. Hutcheon, I. D. Miller, S. Payne, F. Chilcott, S. Waikar, T. Whitaker, A. K. Ah-See, O. Eremin, S. D. Heys, F. J. Gilbert, and P. F. Sharp, "Positron emission tomography using [(18)F]-fluorodeoxy-d-glucose to predict the pathologic response of breast cancer to primary chemotherapy," *J. Clin. Onc.* 18 (2000): 1676–1688.

[4] Wahl, R. L., K. Zasadny, M. Helvie, G. D. Hutchins, B. Weber, and R. Cody, "Metabolic monitoring of breast cancer chemohormonotherapy using positron emission tomography: initial evaluation," *J. Clin. Onc.* 11 (1993): 2101–2111.

[5] Schelling, M., N. Avril, J. Nahrig, W. Kuhn, W. Romer, D. Sattler, M. Werner, J. Dose, F. Janicke, H. Graeff, and M. Schwaiger, "Positron emission tomography using [f-18]fluorodeoxyglucose for monitoring primary chemotherapy in breast cancer," *J. Clin. Oncol.* 18 (2000): 1689–1695.

[6] Mankoff, D. A., L. K. Dunnwald, J. R. Gralow, G. K. Ellis, E. K. Schubert, J. Tseng, T. J. Lawton, H. M. Linden, and R. B. Livingston, "Changes in blood flow and metabolism in locally advanced breast cancer treated with neoadjuvant chemotherapy," *J. Nucl. Med.* 44 (2003): 1806–1814.

[7] Gennari, A., S. Donati, and B. A. Salvadori, "Role of 2-[18F] fluorodeoxyglucose(FDG) positron emission tomography (PET) in the early assessment of response to chemotherapy in metastatic breast cancer patients," *Clinical Breast Cancer* 1 (2000): 156–161.

[8] Choe, R., A. Corlu, K. Lee, T. Durduran, S. D. Konecky, M. Grosicka-Koptyra, S. R. Arridge, B. J. Czerniecki, D. L. Fraker, A. DeMichele, B. Chance, M. A. Rosen, and A. G. Yodh, "Diffuse optical tomography of breast cancer during neoadjuvant chemotherapy: a case study with comparison to MRI," *Med. Phys.* 32(4) (2005): 1128–1139.

[9] Jakubowski, D. B., A. E. Cerussi, F. Bevilacqua, N. Shah, D. Hsiang, J. Butler, and B. J. Tromberg, "Monitoring neoadjuvant chemotherapy in breast cancer using quantitative diffuse optical spectroscopy: a case study," *J. Biomed. Opt.* 9 (2004): 230–238.

[10] Zhu, Q., S. H. Kurtzma, P. Hegde, S. Tannenbaum, M. Kane, M. Huang, N. G. Chen, B. Jagjivan, and K. Zarfos, "Utilizing optical tomography with ultrasound localization to image heterogeneous hemoglobin distribution in large breast cancers," *Neoplasia* 7(3) (2005): 263–270.

[11] Emmenegger, U., G. C. Morton, G. Francia, Y. Shaked, M. Franco, A. Weinerman, S. Man, and R. S. Kerbel, "Low-dose metronomic daily cyclophosphamide and weekly tirapazamine: a well-tolerated combination regimen with enhanced efficacy that exploits tumor hypoxia," *Cancer Research* 66 (2006): 1664–1674.

[12] Warenius, H. M., R. White, J. H. Peacock, J. Hanson, R. A. Britten, and D. Murray, "The influence of hypoxia on the relative sensitivity of human tumor cells to 62.5 MeV (p to Be) fast neutrons and MeV photons," *Radiation Research* 154 (2000): 54–63.

[13] Vaupel, P., and M. Hockel, "Blood supply, oxygenation status and metabolic micromilieu of breast cancers: characterization and therapeutic relevance (review)," *Int. J. Oncol.* 17 (2000): 869–879.

[14] Brown, J. M., "The hypoxic cell: a target for selective cancer therapy (eighteenth Bruce F. Cain memorial award lecture," *Cancer Research* 59 (1999): 5863–5870.

[15] Hockel, M., and P. Vaupel, "Tumor hypoxia: definitions and current clinical, biologic, and molecular aspects," *J. Natl. Cancer Inst.* 93 (2001): 266–276.

[16] Blagosklonny, M. V., "Hypoxia-inducible factor: Achilles heel of antiangiogenic cancer therapy," *Int. J. Oncol.* 19 (2001): 257–262.

[17] Moeller, B. J., Y. Cao, Z. Vujaskovic, C. Y. Li, Z. A. Haroon, and M. W. Dewhirst, "The relationship between hypoxia and angiogenesis," *Sem. Rad. Onc.* 14 (2004): 215–221.

[18] Denny, W. A., "Prospects for hypoxia-activated anticancer drugs," *Curr. Med. Chem. Anti-Canc. Agents* 4 (2004): 395–399.

[19] Rajendran, J. G., D. A. Mankoff, F. O'Sullivan, L. M. Peterson, D. L. Schwartz, E. U. Conrad, A. M. Spence, M. Muzi, D. G. Farwell, and K. A. Krohn, "Hypoxia and Glucose Metabolism in Malignant Tumors Evaluation by [18F] Fluoromisonidazole and [18F] Fluorodeoxyglucose Positron Emission Tomography Imaging," *Clin. Canc. Res.* 10 (2004): 2245–2252.

[20] Padhani, A. R., K. A. Krohn, J. S. Lewis, and M. Alber, "Imaging oxygenation of human tumours," *European Radiology* 17(4) (2007): 861–872.

[21] Thorwarth, D., S. M. Eschmann, F. Paulsen, and M. Alber, "A kinetic model for dynamic [18 F]-Fmiso PET data to analyse tumour hypoxia," *Phys. Med. Biol.* 50(10) (2005): 2209–2224.

[22] Zhou, C., R. Choe, N. Shah, T. Durduran, G. Q. Yu, A. Durkin, D. Hsiang, R. Mehta, J. Butler, A. Cerussi, B. J. Tromberg, and A. G. Yodh, "Diffuse optical monitoring of blood flow and oxygenation in human breast cancer during early stages of neoadjuvant chemotherapy," *J. Biomed. Opt.* 12 (2007): 051903.

[23] Zasadny, K. R., M. Tatsumi, and R. L. Wahl, "FDG metabolism and uptake versus blood flow in women with untreated primary breast cancers," *Eur. J. Nuc. Med. Mol. Imag.* 30 (2003): 274–280.

[24] Tseng, J., L. K. Dunnwald, E. K. Schubert, J. M. Link, S. Minoshima, M. Muzi, and D. A. Mankoff, "18F-FDG kinetics in locally advanced breast cancer: correlation with tumor blood flow and changes in response to neoadjuvant chemotherapy," *J. Nucl. Med.* 45 (2004): 1829–1837.

[25] Konecky, S. D., R. Choe, A. Corlu, K. Lee, R. Wiener, S. M. Srinivas, J. R. Saffer, R. Freifelder, J. S. Karp, N. Hajjioui, F. Azar, and A. G. Yodh, "Comparison of diffuse optical tomography of human breast with whole-body and breast-only positron emission tomography," *Med. Phys.* 35(2) (2008): 446–455.

[26] Corlu, A., R. Choe, T. Durduran, M. A. Rosen, M. Schweiger, S. R. Arridge, M. D. Schnall, and A. G. Yodh, "Three-dimensional in vivo fluorescence diffuse optical tomography of breast cancer in humans," *Opt. Exp.* 15(11) (2007): 6696–6716.

[27] Wernick, M. N., and J. N. Aarsvold, eds., *Emission Tomography: The Fundamentals of PET and SPECT*, New York: Elsevier Academic Press, 2004.

[28] Shepp, L. A., and Y. Vardi, "Maximum likelihood reconstruction for emission tomography," *IEEE Trans. Med. Imag.* 1 (1982): 113–122.

[29] Lange, K., and R. Carson, "EM reconstruction algorithms for emission and transmission tomography," *J. Comput. Assist. Tomogr.* 8 (1984): 306–316.

[30] Browne, J. A., and A. R. De Pierro, "A row-action alternative to the EM algorithm for maximizing likelihoods in emission romography," *IEEE Trans. Med. Imag.* 15 (1996): 687–699.

[31] Surti, S., and J. S. Karp, "Imaging characteristics of a 3-D GSO whole-body PET camera," *J. Nucl. Med.* 45 (2004): 1040–1049.

[32] Freifelder, R., and J. S. Karp, "Dedicated PET scanners for breast imaging," *Phys. Med. Biol.* 42 (1997): 2453–2480.

[33] Freifelder, R., C. Cardi, I. Grigoras, J. R. Saffer, and J. S. Karp, "First results of a dedicated breast PET imager, BPET, using NaI(Tl) curve plate detectors," *IEEE Nuclear Science Symposium Conference Record* 3 (2001): 1241–1245.

[34] Srinivas, S. M., R. Freifelder, J. R. Saffer, C. A. Cardi, M. J. Geagan, M. E.Werner, A. R. Kent, A. Alavi, M. D. Schnall, and J. S. Karp, "A dedicated breast positron emission tomography (BPET) scanner: characterization and pilot patient study," *IEEE Nuclear Science Symposium and Medical Imaging Conference Record*, (San Diego, CA), (2006).

[35] Ntziachristos, V., A. G. Yodh, M. Schnall, and B. Chance, "Concurrent MRI and diffuse optical tomography of breast after indocyanine green enhancement," *Proc. Natl. Acad. Sci.* 97 (2000): 2767–2772.

[36] Hsiang, D., N. Shah, H. Yu, M. Su, A. Cerussi, J. Butler, C. Baick, R. Mehta, O. Nalcioglu, and B. Tromberg, "Coregistration of dynamic contrast enhanced MRI and broadband diffuse optical spectroscopy for characterizing breast cancer," *Technol. Cancer Res. Treat.* 4 (2005): 549–558.

[37] Brooksby, B., B. W. Pogue, S. Jiang, H. Dehghani, S. Srinivasan, C. Kogel, T. D. Tosteson, J.Weaver, S. P. Poplack, and K. D. Paulsen, "Imaging breast adipose and fibroglandular tissue molecular signatures using hybrid MRI-guided near-infrared spectral tomography," *Proc. Natl. Acad. Sci.* 103, pp. 8828–8833, (2006).

[38] Li, A., E. L. Miller, M. E. Kilmer, T. J. Brukilacchio, T. Chaves, J. Stott, Q. Zhang, T. Wu, M. Chorlton, R. H. Moore, D. B. Kopans, and D. A. Boas, "Tomographic optical breast imaging guided by three-dimensional mammography," *Appl. Opt.* 42 (2003): 5181–5190.

[39] Yang, Y. S., H. L. Liu, X. D. Li, and B. Chance, "Low-cost frequency-domain photon migration instrument for tissue spectroscopy, oximetry, and imaging," *Opt. Eng.* 36(5) (1997): 1562–1569.

[40] http://www.medphys.ucl.ac.uk/~martins/toast/index.html, accessed January 2007.

[41] Corlu, A.,R. Choe, T. Durduran, M. Schweiger, E. M. C. Hillman, S. R. Arridge, and A. G. Yodh, "Diffuse optical tomography with spectral constraints and wavelength optimization," *Appl. Opt.* 44(11) (2005): 2082–2093.

[42] Yodh, A. G., and D. A. Boas, "Functional imaging with diffusing light," in *Biomedical Photonics Handbook*, T. Vo-Dinh, (ed.), Boca Raton, FL: CRC Press, 2003, pp. 21-1–21-45.

[43] Bevilacqua, F., A. J. Berger, A. E. Cerussi, D. Jakubowski, and B. J. Tromberg, "Broadband absorption spectroscopy in turbid media by combined frequency-domain and steady-state methods," *Appl. Opt.* 39 (2000): 6498–6507.

[44] J. R. Mourant, T. Fuselier, J. Boyer, T. M. Johnson, and I. J. Bigio, "Predictions and measurements of scattering and absorption over broad wavelength ranges in tissue phantoms," *Appl. Opt.* 36 (1997): 949–957.

[45] Woodard, H. Q., and D. R. White, "The composition of body tissues," *Br. J. Radiol.* 59 (1986): pp. 1209–1219.

[46] White, D. R., H. Q. Woodard, and S. M. Hammond, "Average soft-tissue and bone models for use in radiation dosimetry," *Br. J. Radiol.* 60 (1987): 907–913.

[47] Lee, N. A., H. Rusinek, J. C. Weinreb, R. Chandra, R. C. Singer, and G. M. Newstead, "Fatty and fibroglandular tissue volumes in the breasts of women 20-83 years old: comparison of x-ray mammography and computer-assisted MR imaging," *Am. J. Roentgenology* 168 (1997): 501–506.

[48] Kuwana, E., and E. M. Sevick-Muraca, "Fluorescence lifetime spectroscopy for ph sensing in scattering media," *Anal. Chem.* 75 (2003): 4325–4329.

[49] Lakowicz, J., H. Szmacinski, K. Nowaczyk, W. J. Lederer, M. S. Kirby, and M. L. Johnson, "Fluoroscence lifetime imaging of intracellular calcium in cos cells using quin-2," *Cell Calcium* 15 (1994): 7–27.

[50] Tung, W. R. C., U. Mahmood, and A. Bogdanov, "In vivo imaging of tumors with proteaseactivated near-infrared fluorescent probes," *Nat. Biotechnol.* 17 (1999): 375–378.

[51] Ntziachristos, V., C. Tung, C. Bremer, and W. R. Weissleder, "Fluorescence molecular tomography resolves protease activity in vivo," *Nat. Med.* 8, pp. 757–760, (2002).

[52] Ke, S., X. Wen, M. Gurfinkel, C. Charnsangavej, S. Wallace, E. M. Sevick-Muraca, and C. Li, "Near-infrared optical imaging of epidermal growth factor receptor in breast cancer xenografts," *Cancer Res.* 63 (2003): 7870–7875.

[53] Foster, T. H., B. D. Pearson, S. Mitra, and C. E. Bigelow, "Fluorescence anisotropy imaging reveals localization of meso-tetrahydroxyphenyl chlorin in the nuclear envelope," *Photochem. Photobiol.* 81 (2005): 1544–1547.

[54] Ballou, B., G. W. Fisher, A. S. Waggoner, D. L. Farkas, J. M. Reiland, R. Jaffe, R. B. Mujumdar, S. R. Mujumdar, and T. R. Hakala, "Tumor labeling in vivo using cyanine-conjugated monoclonal antibodies," *Cancer Immunol. Immunother.* 41 (1995): 257–263.

[55] Achilefu, S., R. B. Dorshow, J. E. Bugaj, and R. R., "Novel receptor-targeted fluorescent contrast agents for in vivo tumor imaging," *Invest. Radiol.* 35 (2000): 479–485.

[56] Kwon, S., S. Ke, J. P. Houston, W. Wang, Q. Wu, C. Li, and E. M. Sevick-Muraca, "Imaging dose-dependent pharmacokinetics of an rgd-fluorescent dye conjugate targeted to alpha v beta 3 receptor expressed in Kaposi's sarcoma," *Mol. Imaging.* 4 (2005): 75–87.

[57] O'Leary, M. A., D. A. Boas, B. Chance, and A. G. Yodh, "Reradiation and imaging of diffuse photon density waves using fluorescent inhomogeneities," *J. Lumin.* 60 (1994): 281–286.

[58] O'Leary, M. A., D. A. Boas, X. D. Li, B. Chance, and A. G. Yodh, "Fluorescent lifetime imaging in turbid media," *Opt. Lett.* 21 (1996): 158–160.

[59] Wu, J., L. Perelman, R. R. Dasari, and M. S. Feld, "Fluorescence tomographic imaging in turbid media using early-arriving photons and Laplace transforms," *Proc. Natl. Acad. Sci.* 94 (1997): 8783–8788.

[60] Das, B. B., F. Liu, and R. R. Alfano, "Time-resolved fluorescence and photon migration studies in biomedical and model random media," *Rep. Prog. Phys.* 60 (1997) 227–292.

[61] Hull, E. L., M. G. Nichols, and T. H. Foster, "Localization of luminescent inhomogeneities in turbid media with spatially resolved measurements of CW diffuse luminescence emittance," *Appl. Opt.* 37 (1998): 2755–2765.

[62] Intes, X., J. Ripoll, Y. Chen, S. Nioka, A. G. Yodh, and B. Chance, "In vivo continuous-wave optical breast imaging enhanced with indocyanine green," *Med. Phys.* 30 (2003): 1039–1047.

[63] Corlu, A., R. Choe, T. Durduran, M. A. Rosen, M. Schweiger, S. R. Arridge, M. D. Schnall, and A. G. Yodh, "Three-dimensional in vivo fluorescence diffuse optical tomography of breast cancer in humans," *Opt. Exp.* 15(11) (2007): 6696–6716.

[64] Ntziachristos, V., and W. R. Weissleder, "Experimental three-dimensional fluorescence reconstruction of diffuse media by use of a normalized born approximation," *Opt. Lett.* 26 (2001): 893–895.

[65] Schweiger, M., S. R. Arridge, and I. Nissila, "Gauss-Newton method for image reconstruction in diffuse optical tomography," *Phys. Med. Biol.* 50 (2005): 2365–2386.

[66] Prahl, S., "Optical properties spectra," http://omlc.ogi.edu/spectra/index.html, 2001, accessed February 2008.

[67] Sevick-Muraca, E., G. Lopez, J. Reynolds, T. Troy, and C. Hutchinson, "Fluorescence and absorption contrast mechanisms for biomedical optical imaging using frequency-domain techniques," *Photochem. Photobiol.* 66 (1997): 55–64.

[68] Shah, N., J. Gibbs, D. Wolverton, A. Gerussi, N. Hylton, and B. J. Tromberg, "Combining diffuse optical spectroscopy and contrast-enhanced magnetic resonance imaging for monitoring breast cancer neoadjuvant chemotherapy: a case study," *J. Biomed. Opt.* 10 (2005): 051503.

[69] Pogue, B. W., S. P. Poplack, T. O. McBride, W. A.Wells, K. S. Osterman, U. L. Osterberg, and K. D. Paulsen, "Quantitative hemoglobin tomography with diffuse near-infrared spectroscopy: Pilot results in the breast," *Radiology* 218 (2001): 261–266.

[70] Gu, X. J., Q. Z. Zhang, M. Bartlett, L. Schutz, L. L. Fajardo, and H. B. Jiang, "Differentiation of cysts from solid tumors in the breast with diffuse optical tomography," *Acad. Radiol.* 11 (2004): 53–60.

[71] Pifferi, A., P. Taroni, A. Torricelli, F. Messina, R. Cubeddu, and G. Danesini, "Four-wavelength time-resolved optical mammography in the 680-980-nm range," *Opt. Lett.* 28 (2003): 1138–1140.

[72] Zhu, Q., E. Conant, and B. Chance, "Optical imaging as an adjunct to sonograph in differentiating benign from malignant breast lesions," *J. Biomed. Opt.* 5(2) (2000): 229–236.

[73] Azar, F. S., K. Lee, A. Khamene, R. Choe, A. Corlu, S. D. Konecky, F. Sauer, and A. G. Yodh, "Standardized platform for coregistration of nonconcurrent diffuse optical and magnetic resonance breast images obtained in different geometries," *J. Biomed. Opt.* 12 (2007).

[74] Holboke, M. J., B. J. Tromberg, X. Li, N. Shah, J. Fishkin, D. Kidney, J. Butler, B. Chance, and A. G. Yodh, "Three-dimensional diffuse optical mammography with ultrasound localization in a human subject," *J. Biomed. Opt.* 5 (2000): 237–247.

[75] Zhu, Q. L., M. M. Huang, N. G. Chen, K. Zarfos, B. Jagjivan, M. Kane, P. Hedge, and S. H. Kurtzman, "Ultrasound-guided optical tomographic imaging of malignant and benign breast lesions: Initial clinical results of 19 cases," *Neoplasia* 5 (2003): 379–388.

[76] Zhang, Q., T. J. Brukilacchio, A. Li, J. J. Stott, T. Chaves, E. Hillman, T. Wu, A. Chorlton, E. Rafferty, R. H. Moore, D. B. Kopans, and D. A. Boas, "Coregistered tomographic x-ray and optical breast imaging: initial results," *J. Biomed. Opt.* 10(2) (2005): 024033.

[77] Graves, E. E., J. Ripoll, R. Weissleder, and V. Ntziachristos, "A submillimeter resolution fluorescence molecular imaging system for small animal imaging," *Med. Phys.* 30 (2003): 901.

[78] Pogue, B. W., S. L. Gibbs, B. Chen, and M. Savellano, "Fluorescence imaging in vivo: raster scanned point-source imaging provides more accurate quantification than broad beam geometries," *Technol. Cancer Res. Treat.* 3 (2004): 15–21.

[79] Patwardhan, S. V., S. R. Bloch, S. Achilefu, and J. P. Culver, "Time-dependent whole-body fluorescence tomography of probe bio-distributions in mice," *Opt. Express* 13 (2005): 2564–2577.

[80] Hwang, K., J. P. Houston, J. C. Rasmussen, A. Joshi, S. Ke, C. Li, and E. M. Sevick-Muraca, "Improved excitation light rejection enhances small-animal fluorescent optical imaging," *Mol. Imaging* 4 (2005): 194–204.

[81] Bloch, S., F. Lesage, L. McIntosh, A. Gandjbakhche, K. Liang, and S. Achilefu, "Whole-body fluorescence lifetime imaging of a tumor-targeted near-infrared molecular probe in mice," *J. Biomed. Opt.* 10 (2005): 54003.

[82] Kwon, S., and E. M. Sevick-Muraca, "Non-invasive imaging of lymph propulsion in mice," *Lymphatic Research and Biology* 5 (2007): 219–231.

[83] Sharma, R., W. Wang, J. C. Rasmussen, A. Joshi, J. P. Houston, K. E. Adams, A. Cameron, S. Ke, M. E. Mawad, and E. M. Sevick-Muraca, "Quantitative lymph imaging," *Am. J. Physiol. Heart Circ. Physiol.* 292 (2007): 3109–3118.

[84] Sevick-Muraca, E. M., R. Sharma, J. C. Rasmussen, M. V. Marshall, J. A. Wendt, H. Q. Pham, E. Bonefas, J. P. Houston, L. Sampath, K. E. Adams, D. K. Blanchard, R. E. Fisher, S. B. Chiang, R. Elledge, and M. E. Mawad, "Imaging of lymph flow in breast cancer patients after microdose administration of a near-infrared fluorophore: feasibility study," *Radiology* 246 (2008): 734–741.